The role of backscattered energetic atoms in film growth in reactive magnetron sputtering of chromium nitride

2007 J. Phys. D: Appl. Phys. 40 778

(http://iopscience.iop.org/0022-3727/40/3/014)

INSTITUTE OF PHYSICS PUBLISHING JOURNAL OF PHYSICS D: APPLIED PHYSICS

J. Phys. D: Appl. Phys. **40** (2007) 778–785 doi:10.1088/0022-3727/40/3/014

The role of backscattered energetic atoms in film growth in reactive magnetron sputtering of chromium nitride

K Sarakinos, J Alami, P M Karimi, D Severin and M Wuttig

Institute of Physics (IA), RWTH Aachen University of Technology, 52056 Aachen, Germany

E-mail: ksara@physik.rwth-aachen.de

Received 12 July 2006, in final form 5 December 2006
Published 19 January 2007
Online at stacks.iop.org/JPhysD/40/778

Abstract

In this work the impact of backscattered energetic atoms on film growth in reactive sputtering of CrN_x ($x \leqslant 1$) is manifested. We use film and plasma characterization techniques, as well as simulations in order to study the dynamics of the target–discharge–film interactions. The results show that the primary bombarding species of the growing film are N_2^+ plasma ions, which are neutralized and backscattered by the target in the form of atomic N. It is shown that the backscattered N atoms have energies which are significantly higher than those of other bombarding species, i.e. the backscattered Ar atoms, the sputtered atoms and the plasma ions. Moreover, it is found that CrN films exhibit compressive stresses of 2.6 GPa and a density close to the bulk value. We attribute these properties to the bombardment by backscattered energetic atoms, in particular N. Pure Cr films are also studied for reference.

1. Introduction

Chromium nitride (Cr_2N, CrN) thin films have attracted significant scientific and technological interest during the last decade, since they exhibit relatively high hardness and chemical stability [1–3]. As a result, they are used as hard and protective coatings in severe environments. A number of reports on the growth of chromium nitrides employing the PVD [4–13] and CVD [14] techniques are available in the literature. In these studies reactive magnetron sputtering from an elemental Cr target in an Ar–N_2 atmosphere is frequently used. By varying the composition of the working gas, i.e. the partial pressures of Ar and N_2, films with different stoichiometries and phase compositions are obtained [5–10]. In addition, when the target-to-substrate distance, the working gas pressure and the target power are varied, the bombardment regime during growth, i.e. the energy and the flux of the neutral and ionized species that impinge on the growing film, can be tailored. This, in turn, enables the manipulation of the films' structural, nanomechanical and tribological properties [5–10, 15]. In addition the energy of the ionized bombarding species can also be controlled by applying a negative substrate voltage [5–10, 15]. The gas composition can also affect the bombardment regime during the growth. Petrov *et al* [16] showed that in Ar–N_2 discharges N_2^+ ions become the dominant charged species as the N_2 partial pressure exceeds 75% of the total working pressure. In addition, Wang *et al* [17] reported that N_2^+ ions undergo dissociative neutralization, when they impinge on the target, giving rise to two N atoms, which are, then, backscattered. The energy of the impinging ions depends on the target voltage which is between 300 and 500 V for most dc magnetron sputtering processes. Upon collision with the target, and depending on the mass of the target atoms and the impinging ions, a fraction of this energy is transferred to the backscattered species [16, 17]. Petrov *et al* [16] showed that the backscattered N species have much higher energies than the sputtered atoms. However, the effect of the backscattered species on the growth of CrN films and the resulting film properties is yet to be investigated.

In the present work simulations based on the Berg's model [18] for reactive deposition are employed in order to link the target and the film properties. The results of these simulations are combined with computations using the TRIM freeware [19] in order to investigate the interactions of the plasma ions with the target. Moreover, Langmuir probe measurements are performed in order to obtain information about the energy

of the ionized plasma species that impinge on the growing film. Finally, TRIM computations are also used to study the interactions of the plasma species with the growing films. We identify, thus, the relationship between the working gas composition, the bombarding regime of the growing film and the resulting film structural properties. This enables us to establish the role of the backscattered energetic atoms during reactive growth of CrN films.

2. Experimental procedure

CrN_x ($x \leqslant 1$) films were deposited on c-Si (1 0 0), glass and graphite substrates employing dc reactive magnetron sputtering in a balanced configuration. The magnetic field strength was 200 G at the centre of the target and the zero magnetic field distance was calculated using the FEEM freeware [20] to be ∼40 mm. A Cr target (cathode) with a diameter of 76 mm and a purity of 99.95% was used. The substrates were placed 70 mm above the centre of the target and were grounded. Prior to deposition the chamber was evacuated to a base pressure of $p_b \sim 10^{-6}$ mbar. The depositions were carried out in a mixed Ar–N_2 ambient. The N_2 flow (q_{N_2}) was varied between 0 and 50 sccm and the Ar flow was adjusted in order to hold a constant working pressure of 0.8×10^{-2} mbar. The target was operated at a constant current of 900 mA. The substrate temperature was measured by a pt-100 thermo-resistor clamped on the substrate holder and was found to be ∼160 °C at all deposition conditions.

The composition of the films for the various q_{N_2} values was determined by Rutherford backscattering spectroscopy (RBS). A tandetron accelerator was used with 1.4 MeV $^4He^+$ particles and a current of 14 mA. The backscattered $^4He^+$ particles were detected by a semiconductor detector positioned at an angle of 170° with respect to the incident beam direction. The RBS spectra were analysed using the XRUMP [21] software. The RBS measurements were performed for samples grown on graphite substrates in order to decrease the overlap of substrate and film spectra and to improve the resolution capability for low cross-section elements like N.

X-ray measurements were carried out for samples grown on c-Si (1 0 0) as well as glass substrates using a Philips X'Pert Diffractometer. X-ray reflectometry (XRR) was employed in order to determine the film thickness and consequently also the deposition rate. In addition, XRR was also used for the calculation of the film density and the roughness both at the surface and at the interface. The crystal structure and the phase composition of the films were investigated by means of x-ray diffraction (XRD). The XRD measurements were performed in both Bragg–Brentano (BB) and grazing incidence (GI) geometry.

The residual stresses of the films were also investigated. In general, the residual stresses can be either compressive or tensile [22]. The compressive stresses are related to the energetic bombardment and caused both by the direct subplantation of bombarding species in the films and/or by the displacement of film lattice atoms to interstitial positions [23, 24]. The tensile stresses are generated due to the shrinkage of the grain boundaries [25]. In addition, the magnitude of the residual stresses can be affected by the growth temperature. The deposition of thin films at temperatures different from the ambient temperature causes the so-called thermal stresses σ_{th} which can be calculated by the equation [22]

$$\sigma_{th} = \frac{E_f}{1 - \upsilon_f}(a_f - a_s)\Delta T, \tag{1}$$

where E_f and υ_f are the bulk modulus and the Poisson's ratio of the film, a_f and a_s the thermal expansion coefficient of the film and the substrate, respectively, and ΔT the difference between the growth and ambient temperature. The thermal stresses can be either compressive or tensile depending on the sign of the terms $a_f - a_s$ and ΔT in equation (1). The residual stresses for our films were determined by analysing films grown on 150 μm glass substrates with a biaxial modulus of 92 GPa. The substrate curvature was measured before and after deposition and the stresses were calculated using Stoney's formula [26]. The effect of the residual stresses on the film strain was investigated utilizing the $\sin^2\psi$ method proposed by Perry [27]. According to this method, the stress–strain relation in a film as a function of the orientation of the lattice planes with respect to the surface of the sample is described by the equation

$$\varepsilon = \frac{d^{\psi}_{hkl} - d^{0}_{hkl}}{d^{0}_{hkl}} = \frac{1+\nu}{E}\sigma \sin^2\psi - 2\frac{\nu}{E}\sigma, \tag{2}$$

where ε is the film strain, d^{ψ}_{hkl} is the d-spacing of the (hkl) planes oriented at various tilt angles ψ with respect to the BB geometry, d^{0}_{hkl} is the d-spacing value obtained by the BB geometry ($\psi = 0$, planes parallel to the surface), ν and E are the Poisson's ratio and the elastic modulus of the analysed film, respectively, and σ is the value of the residual stresses. Equation (2) implies that $\sigma_{xx} = \sigma_{yy} = \sigma$. Here σ_{xx} and σ_{yy} are the two components of the in-plane biaxial stresses, i.e. the stresses on the sample surface.

In order to investigate the discharge characteristics, plasma characterization was carried out, at 40 mm from the target surface, using a cylindrical Langmuir probe consisting of a tungsten wire of length $l_{pr} = 5.0 \pm 0.5$ mm and radius $r_{pr} = 0.05 \pm 0.01$ mm. Details of the probe construction are found elsewhere [28]. Voltage values V between −15 and 15 V were applied to the probe and the probe current I was measured over a resistor of 100 Ω. The probe I–V curves were analysed using the second derivative method proposed by Lieberman and Lichtenberg [29], and plasma characteristics, such as the plasma (electron) density and the plasma potential were obtained.

3. Simulation details

The target–discharge–film interactions upon the reactive sputtering of the CrN_x films are depicted in figure 1. It is shown that a fraction of the target surface is covered (nitrified) by Cr–N compounds. In general, it is known that in the reactive sputtering the composition of the target surface (target coverage) and the sample stoichiometry differ [18, 30, 31]. In particular, at the same deposition conditions, a lower fraction of the reactive element atoms is expected on the target surface than in the film [18, 30, 31]. In order to support the validity

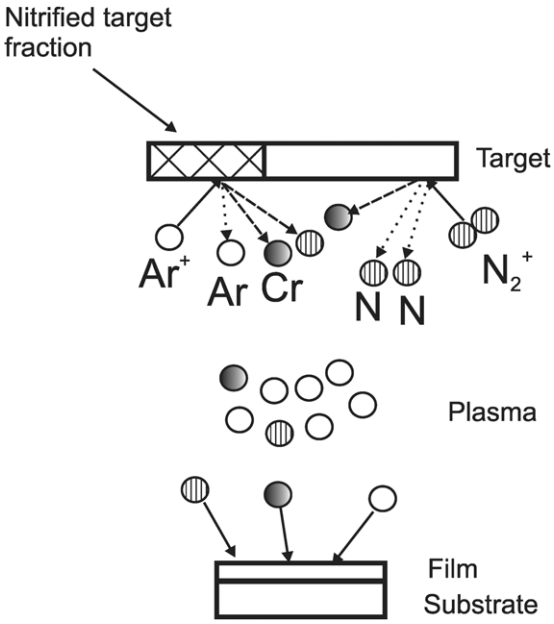

Figure 1. Target–discharge–film interactions upon the reactive sputtering of CrN_x films.

of this statement the Berg's model for reactive deposition was used [18]. Process characteristics, such as the target voltage (V_T), the deposition rate (derived from XRR) and the sample stoichiometry (derived from RBS) as a function of the N_2 flow were fitted to the rate equations, as described by Berg *et al* [18,32] and the target coverage θ_t was obtained for the different N_2 flows. Other fundamental processes during the reactive sputtering of CrN_x films, such as the impingement of plasma ions (Ar^+ and N_2^+) on the target (solid arrows), are also depicted in figure 1. Upon impingement these ions are neutralized via an inverse Auger process [16] and backscattered (dotted arrows). In addition, atoms from the target surface are sputtered (dashed arrows). The flux of the backscattered and sputtered species is transmitted through the plasma gas undergoing collisions with the plasma particles. Finally, the transmitted species impinge on the growing film.

The dynamics of the interactions described in figure 1 were studied using a three-stage simulation process based on the TRIM freeware [19], which are described in detail in the following paragraphs.

(i) The results of the analysis based on the Berg's model were combined with TRIM computations in order to study the interactions of the plasma ions with the target. In these simulations the deposition conditions (N_2 flow and target voltage) which correspond to the growth of stoichiometric CrN films were considered. In particular, a CrN_x target with mass density $\rho = \theta_t'\rho^{CrN} + (1-\theta_t')\rho^{Cr}$ was considered. Here $x = \theta_t'$ is the target coverage at the deposition conditions of CrN films, calculated by the analysis based on the Berg's model. In addition, ρ^{Cr} and ρ^{CrN} are the bulk densities of Cr [33] and CrN [34], respectively. Upon incidence of the Ar^+ and the N_2^+ ions on the CrN_x target the backscattered particles were studied. The energy of the incident Ar^+ and N_2^+ ions was considered to be equal to the target voltage, i.e. eV_T. Furthermore, the N_2^+ ions are treated according to Wang *et al* [17], who showed that the N_2^+ ions with an energy eV_T much higher that the dissociation energy of the N_2 molecule (9.7 eV) [35, 36] dissociate upon impinging on the target and are backscattered as two N neutrals (see figure 1). For incident ions with energies greater than 100 eV, the dissociation probability approaches unity [17]. Therefore, we considered in our calculations that an impinging N_2^+ ion can be replaced by two N projectiles with energy $eV_T/2$, as proposed by Petrov *et al* [16] and Wang *et al* [17]. The computations provided the energy distributions of the backscattered species and their ratio with respect to the total number of the impinging ions.

(ii) The interactions of the backscattered species with the glow discharge were studied using the TRIM simulations. The glow discharge was described as a gaseous Ar–N 'target'. The width of this target was 70 mm, equal to the actual target-to-substrate distance. An Ar–N_2 target composition was considered, due to the equal partial pressures of the two gases for the deposition conditions of CrN. The mass density of the Ar–N_2 gaseous target that corresponds to a working pressure of 0.8×10^{-2} mbar was calculated to be 1.14×10^{-8} g cm^{-3}. The computations provided the ratio of the transmitted species with respect to the number of the backscattered species and their energy distributions.

(iii) TRIM computations were utilized in order to study the effect of the transmitted species on the growing films. A CrN film with mass density equal to the value determined by the XRR (see section 4.1) was considered. In these computations, the number of lattice interstitials induced per incident particle was calculated. In addition, the ratio of the impinging particles that are subplanted was determined. The subplantation is a process of shallow implantation of hyperthermal species below the growing film's surface introduced by Lifshitz *et al* [37]. The subplantation occurs whenever the projected range of an incident bombarding particle in the film is larger than the width of the film surface [37]. A physically reasonable estimation for the width of the film surface is the thickness of the first monolayer [38]. Here the monolayer thickness was considered to be equal to the CrN primitive cell size [34].

It has to be mentioned here that the above presented simulation process merely provides a qualitative description of the target–plasma–film interactions during the reactive sputtering process. The obtained, by the simulations, quantities are combined with experimental findings regarding the plasma characteristics and the film properties in order to demonstrate trends in the energetic bombardment of the films and to identify the role of the backscattered energetic atoms on film growth. For reference, the dynamics of the film–discharge–target interactions for the growth of Cr films were also studied by using the previously described analysis.

4. Results

4.1. Film and plasma properties

The variation of the film composition x (x = [N]/[Cr] ratio), obtained from the RBS measurements, upon the increase of q_{N_2} is presented in figure 2. It is observed that the ratio x increases with increasing q_{N_2} up to ~30 sccm, where $x \sim 1$. After this point, saturation is observed, i.e. stoichiometric CrN films are obtained. The microstructure of a stoichiometric CrN

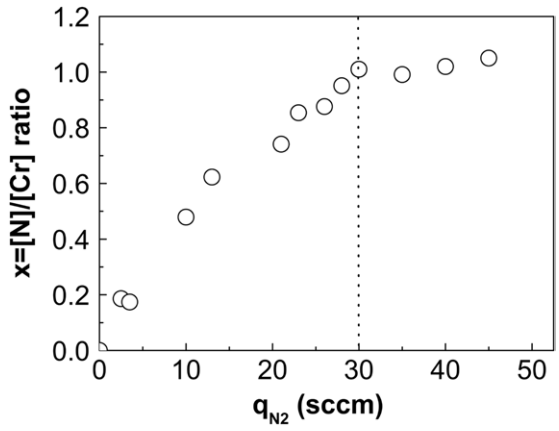

Figure 2. Variation of film composition x (x = [N]/[Cr] ratio) as a function of N_2 flow (q_{N_2}). The vertical dotted line is a guide to the eye.

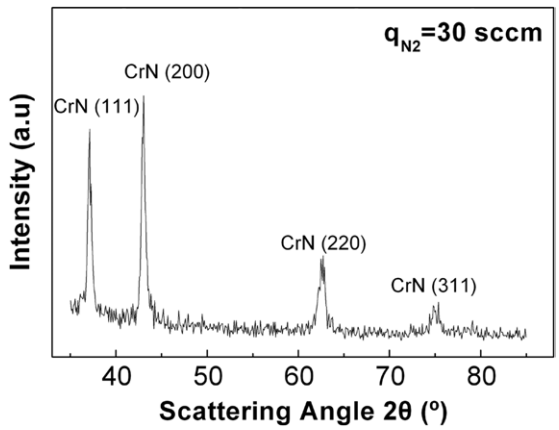

Figure 3. GI-XRD pattern of CrN_x film grown at $q_{N_2} = 30$ sccm. The reflections are attributed to the rocksalt crystal structure of the CrN phase.

Table 1. Crystal structure, phase composition, density and residual stresses for films grown at $q_{N_2} = 30$ and 0 sccm.

q_{N_2} (sccm)	Crystal structure/ phase	Density [bulk values] (g cm^{-3})	Residual stresses (GPa)
30	rocksalt/CrN	6.1 ± 0.01 [6.14]	-2.66 ± 0.02
0	bcc/Cr	6.75 ± 0.02 [7.2]	$+1.55 \pm 0.02$

film grown at $q_{N_2} = 30$ sccm was investigated by means of the GI-XRD. The corresponding GI-XRD pattern is presented in figure 3. The reflections in figure 3 are attributed to the rocksalt crystal structure of the CrN phase [34]. Other properties of the film grown at $q_{N_2} = 30$ sccm, such as the density and the residual stresses, were also investigated. The XRR analysis and the wafer curvature method revealed a density of 6.1 g cm^{-3} ($\rho^{bulk} = 6.14$ g cm^{-3} [34]) and compressive stresses of 2.66 GPa, respectively. The results are summarized in table 1, where the corresponding results for pure Cr are also listed for reference.

Alternatively, the residual stresses of the films were determined by the d–$\sin^2\psi$ method. The results for a CrN film

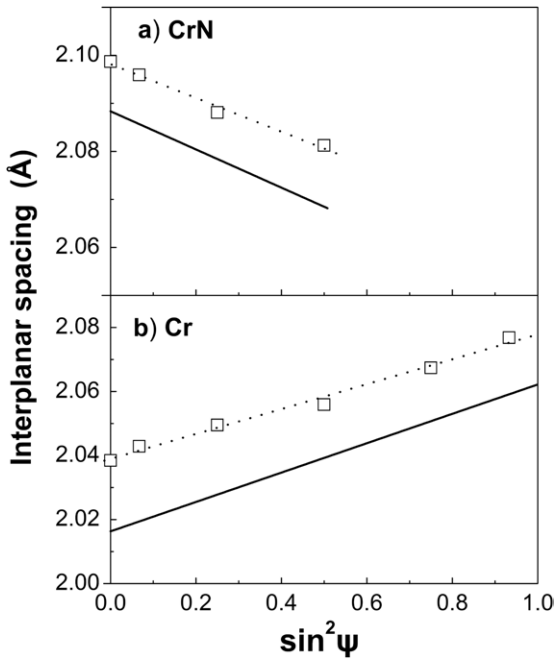

Figure 4. Interplanar spacing d versus $\sin^2\psi$ of the tilt angle ψ of the sample with respect to the BB geometry for (a) CrN and (b) Cr films. The points are the experimental data and the dotted lines their least-square linear fit. The solid lines are the calculated d^{ψ}_{hkl} values for the stress values obtained by the wafer curvature method and the d^{0}_{hkl} value for unstrained bulk CrN and Cr, respectively.

grown at $q_{N_2} = 30$ sccm are presented in figure 4(a). The open squares correspond to the experimental data and the dotted line to their least-square linear fit. The d-spacing values for CrN were calculated from the angular position of the CrN (2 0 0) reflections. The negative slope of the d–$\sin^2\psi$ line in figure 4(a) is indicative of compressive stresses. The magnitude of the stresses was calculated by substituting the slope of the d–$\sin^2\psi$ line and the elastic constants of CrN [15] in equation (2). The calculation yielded compressive stresses of 2.32 GPa that are in good agreement with those obtained by the Stoney's method (2.66 GPa). The solid straight line in figure 4(a) corresponds to d^{ψ}_{hkl} values calculated from equation (2) using as d^{0}_{hkl}, i.e. d^{ψ}_{hkl} for $\psi = 0^{\circ}$, the interplanar spacing of the (2 0 0) planes in unstrained bulk CrN crystal [34] and as σ the residual stresses which were obtained by the wafer curvature method. This corresponds to films under in-plane biaxial stresses, according to the analysis presented by Janssen and Kamminga [39]. Cr films were also studied with the d–$\sin^2\psi$ method (figure 4(b)). The analysis yielded tensile stresses of 1.33 GPa. Moreover, in both figures 4(a) and (b) the solid straight lines are shifted to lower values with respect to the d-spacing determined experimentally.

Finally, the plasma properties at the CrN deposition conditions ($q_{N_2} = 30$ sccm) were determined by means of Langmuir probe measurements. The plasma (electron) density, n_e, was found to be 4.8×10^{15} m^{-3}. This value is typical for dc magnetron processes. In addition, the plasma potential, V_p, was 0.25 V. Similar values were also found for the pure Ar plasma employed to grow Cr films.

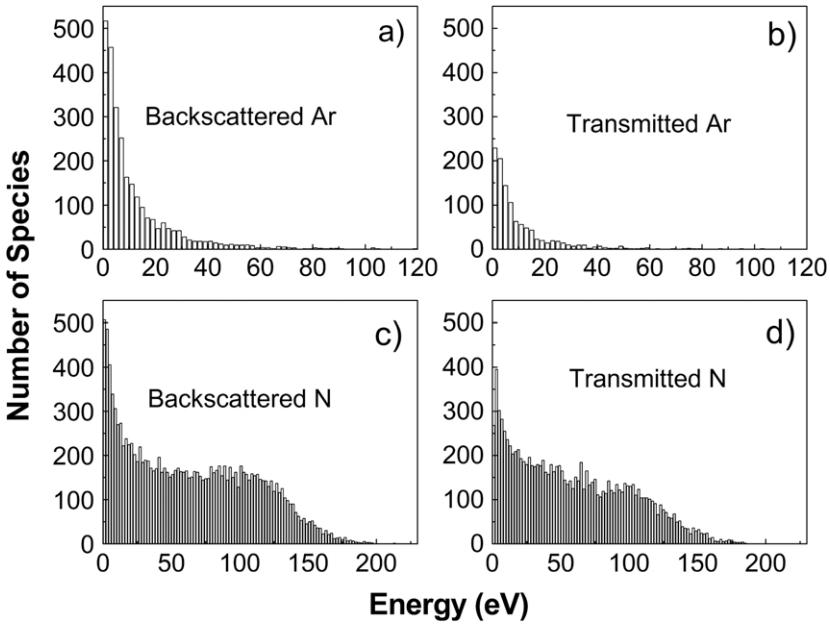

Figure 5. Energy distribution of (*a*) backscattered Ar, (*b*) transmitted Ar, (*c*) backscattered N and (*d*) transmitted N species as provided by the TRIM computations.

Table 2. Results of TRIM computations for the interactions of the plasma ions with Cr–N and Cr targets. R_{back} is the ratio of the backscattered species with respect to the number of the impinging ions and E_{back} their energy.

	R_{back}^{Ar}	E_{back}^{Ar} (eV)	R_{back}^{N}	E_{back}^{N} (eV)
Cr–N	0.026 95	11.74	0.1337	63.19
Cr	0.036 1	9.48	—	—

Table 3. Results of TRIM computations for the interactions of the backscattered species with the plasma. R_{tr} is the ratio of the transmitted species with respect to the number of the backscattered species and E_{tr} their energy.

	R_{tr}^{Ar}	E_{tr}^{Ar} (eV)	R_{tr}^{N}	E_{tr}^{N} (eV)
CrN	0.402	9.99	0.8034	57.97
Cr	0.423	10.76	—	—

4.2. Growth process simulation

The target coverage θ_t at $q_{N_2} = 30$ sccm, i.e. at the CrN growth conditions, was found by the calculations based on the model proposed by Berg and Nyberg [18] to be $\theta_t' \approx 0.4$. This confirms our expectation that the N fraction on the target surface is lower than the N fraction in the sample. The calculated θ_t value was used as the composition of the Cr–N target in the TRIM computations which were employed to study the backscattered Ar and N species (stage (i) in section 3). In the same computations the target voltage, i.e. the energy of the plasma ions that impinge on the target, was $V_T = 504$ V. The energy distributions of the backscattered Ar and N species, as obtained by the TRIM computations, are plotted in figures 5(*a*) and (*c*), respectively. It is evident that the backscattered N species have, on average, a higher energy than the corresponding Ar species, with respective mean energies of ∼63 eV and ∼11 eV. Furthermore, backscattering ratios (R_{back}) of ∼3% and ∼13% were calculated for Ar and N species, respectively. The above presented results are summarized in table 2. It should be pointed out here that for the calculations of the target coverage, which is used in stage (i) of the simulation procedure, the contributions of the N_2^+ and N^+ ions to the sputtering process [30], as well as the implantation of the reactive gas ions in the target [31] were not considered. This affects the accuracy of the calculated θ_t value [30, 31], which in turn determines the average mass of the target atoms and consequently, affects the energy of the backscattered species [16,17], as further discussed in section 5. However, the same θ_t values are used to study both Ar and N backscattered atoms (see section 3). As a result, the previously presented trends regarding the energy of these species will be the same irrespective of the target coverage considered. Simulations of the interactions of the backscattered species with the plasma (stage (ii) of the simulation procedure) revealed transmission ratios R_{tr}, with respect to the number of the backscattered neutrals, of ∼40% and ∼80% for the Ar and N species, respectively. The energy distributions for the transmitted Ar and N species are presented in figures 5(*b*) and (*d*), respectively. Similarly to the backscattered species, the transmitted N species have on average higher energies than the transmitted Ar species, with calculated mean values (E_{tr}) ∼ 57 eV and ∼10 eV, respectively. The results for the transmitted species are summarized in table 3. Finally, simulations of the effect of the transmitted species on the growing film showed that the Ar species have a subplantation ratio of ∼0.3% and do not induce lattice interstitials. On the other hand, the N species have a much higher subplantation ratio of ∼48% and induce 0.4 interstitials per impinging neutral. It shall be pointed out here that the subplantation ratio strongly depends on the monolayer thickness. The latter, in turn, depends on the orientation of the crystallographic planes which are considered. In the present calculations, the goal is to compare the subplantation ratio of the N and the Ar species in a CrN film. For this reason, the

Table 4. Results of TRIM computations regarding the effect of the transmitted neutral species on the film. R_{sub} is the subplantation ratio of the impinging species in the film and I the number of lattice interstitials that they induce.

	R_{sub}^{Ar}	I^{Ar} (/species)	R_{sub}^{N}	I^{N} (/species)
CrN	0.0322	0	0.4865	0.4
Cr	0.12	0	—	—

size of the primitive CrN cell is used as a monolayer thickness. These results are summarized in table 4. In all the cases (tables 2–4) the corresponding results for Cr films are also listed for reference.

5. Discussion

It was shown in section 4 that CrN films exhibit high compressive stresses and a density similar to the bulk value. These properties are typical for films grown under energetic bombardment, e.g. for films grown on negatively biased substrates [15]. In the depositions described in this work, all substrates were grounded. As a consequence, the energy that ionized particles gain upon deposition is eV_p, where V_p is the plasma potential which was determined to be 0.25 V. Furthermore, the number of the ionized species in a dc magnetron sputtering discharge is very low (<1%) [40]. In addition, it is known that the mean energy of the sputtered particles ranges from 2 to 6 eV [41–44] and the majority of them are thermalized. Therefore, the exhibited CrN film properties cannot be attributed to bombardment by plasma ions or sputtered atoms. Moreover, from equation (1) the thermal stresses of the CrN films can be calculated. Using the growth temperature of 160 °C, the elastic constants of CrN [15], and the thermal expansion coefficient for Si [45] and CrN [46], compressive thermal stresses of 0.02 GPa were calculated. This value is significantly lower than the value of the measured compressive stresses (2.66 GPa). Hence, a different mechanism has to be invoked in order to explain the observed film properties.

TRIM computations showed that the N_2^+ species which are backscattered from the target in the form of atomic N have a significantly higher energy than the backscattered Ar species. These findings can be understood within a binary collision model, which describes the normal incidence of a moving plasma ion on a stationary target atom. In particular, the ratio of the energy transferred to the backscattered ion (E_b) with respect to the energy of the incident ion (E_i) is given by the equation

$$\frac{E_b}{E_i} = \left(\frac{m_i - m_t}{m_i + m_t}\right)^2. \tag{3}$$

Here m_i and m_t are the masses of the impinging ions and the target atoms, respectively. By using the atomic masses $m_{Ar} = 40$ amu and $m_N = 14$ amu for the ions and $m_{CrN0.4} = (m_{Cr} + 0.4 \cdot m_N)/1.4 = 41.14$ amu for the $CrN_{0.4}$ target, we have calculated that the energy transfer ratio for Ar is 1%, while the transfer ratio for N is 24%. The results based on the binary collision model are consistent with the results obtained by the simulations. The significantly higher energy of the backscattered N species is due to their relatively smaller mass in comparison to the mass of the Ar species, with respect to the mass of the target atoms. In addition, the trends which are manifested by the TRIM simulations and the binary collision model are also in good agreement with results reported by Petrov *et al* [16].

The interaction of the backscattered particles with the plasma species can also be elucidated by employing the same collision model. In that case the energy loss of a backscattered particle with energy E_i and mass m_i upon collision with a stationary plasma particle with mass m_t is given by the equation

$$\frac{E_t}{E_i} = \frac{4m_i m_t}{(m_i + m_t)^2}, \tag{4}$$

where E_t is the energy of the plasma particle after the collision. The calculations based on equation (4) showed that the energy loss for the Ar and N species is 99% and 82%, respectively. For the calculations we used the corresponding atomic masses for the Ar and N species. In addition, a mass $m_{ArN_2} = (m_{Ar} + m_{N_2})/2 = 34$ amu for the the Ar–N_2 plasma was used. The total energy loss of a transmitted particle depends on the number of collisions that this particle undergoes moving from the target towards the growing film, which in turn depends on the mean free path for momentum transfer, λ. This is given by the equation [29]

$$\lambda = \frac{1}{4\sigma_p n_g}. \tag{5}$$

Here n_g is the molecular density of the plasma gas and σ_p the momentum transfer collision cross-section of the plasma particles. The collision cross-section depends on the size of the gas particles and in a first approximation $\sigma_p = \pi d^2$, where d is the diameter of the particle. The gas density is $n_g = p/kT$, where $p = 0.8 \times 10^{-2}$ mbar is the sputtering pressure. By assuming that the plasma consists of Ar atoms with a diameter of 3 Å [45], a mean free path of ∼13 mm was calculated. This means that the sputtered and backscattered particles undergo on average ∼5 collisions as they move from the target towards the substrate, since the substrate-to-target distance is 70 mm. If we assume that the energy loss is the same for each collision, we can calculate the fraction of the initial energy that a particle possesses after the fifth collision; $(1 - (E_t/E_i))^5$. By using the E_t/E_i values for the backscattered Ar and N species, which were calculated from equation (4), it was found that N atoms posses a 1.5×10^{-4} fraction of their initial energy. This value is higher by 7 orders of magnitude than the corresponding values for the Ar species. These findings manifest the same trends as the simulation results for the transmitted species (table 3), which suggested that 40% and 80%, respectively, of the backscattered Ar and N particles are transmitted. In particular, both the binary collision model and the simulations show that the Ar species are scattered more efficiently than the N species during their transmission through the plasma gas.

Based on the above presented analysis we suggest here that the backscattered N atoms are the major bombarding species during the growth of CrN films. In addition, it is seen that the simulation results regarding the effect of the backscattered species on the CrN films (table 4) correlate well with the experimental findings. In particular, it was found that the backscattered species (mainly N) are subplanted in the film and cause interstitials. The direct subplantation and/or

the displacement of lattice atoms to interstitial positions lead to out-of-plane lattice expansion [47, 48] and generation of compressive stresses [23, 24]. Compressive stresses were found experimentally, both by the wafer curvature and the d–$\sin^2\psi$ methods. In addition, the existence of the out-of-plane lattice expansion is clearly illustrated in figure 4(*a*). It shall be pointed out here that the film stresses obtained both by the wafer curvature and the d–$\sin^2\psi$ methods are in-plane biaxial stresses and the out-of-plane strain that they cause is included in equation (2). Nevertheless, in figure 4(*a*) an offset of the experimental d_{hkl}^{ψ} values with respect to the d_{hkl}^{ψ} values which correspond to a biaxial stressed lattice (solid lines) is observed. This is indicative of an additional out-of-plane lattice expansion. Since the bombarding efficiency of the ionized species and sputtered atoms is low, we attribute the out-of-plane lattice strain and the compressive stresses to the bombardment by the backscattered (mainly N) plasma species.

The same effect, i.e. additional out-of-plane lattice expansion, is also observed in the case of the Cr films (figure 4(*b*)). However, these films exhibit tensile stresses. This contradiction can be elucidated in the light of the additivity of the stress components [39], i.e. tensile stresses generated by the shrinkage of the grain boundaries [25] and compressive stresses generated by the atomic peening [23, 24] are additive in nature. The dominant stress component determines the stress sign of the film. In our case, the TRIM computations show that a fraction of the backscattered Ar^+ ions is subplanted in the Cr films. We argue that this is the reason for the observed out-of-plane lattice expansion, which in turn induces a compressive stress component. On the other hand, the low deposition temperature (∼160 °C), the relatively low energetic bombardment and the fact that Cr is a low mobility metal [49] are indicative of limited surface diffusion of the adatoms [50]. This can explain the low density of the Cr films. Low density structures, on the other hand, exhibit voids and extended grain boundaries [38], which lead to tensile stresses [25]. The positive (tensile) stress sign in our Cr films implies that the tensile stress term caused by the shrinkage of the grain boundaries cannot be compensated by the compressive stress term caused by the subplantation of the backscattered Ar species.

6. Conclusions

In this work experimental techniques and simulations were used in order to study the role of backscattered plasma species in film growth in the reactive magnetron sputtering of CrN. It was shown that the neutralized plasma ions that are backscattered by the target impinge to the substrate with a significantly higher energy than the corresponding ionized plasma species. In addition, it was found by simulations that the energy of backscattered N_2^+ species, in the form of atomic N, is significantly higher than that of the Ar species. This was explained by the lower mass of N with respect to the mass of the target atoms and the plasma species compared with that of Ar. Out-of-plane lattice strain and compressive stresses were found experimentally for the CrN films. This was attributed to the subplantation of backscattered N species, as the simulations results showed. Cr films were also studied for reference. A less intense bombardment by the backscattered Ar ions, compared with the CrN films, was found by the simulations. This is consistent with the formation of underdense film and the tensile stresses found experimentally. Furthermore, the simulations showed that a fraction of the backscattered Ar species is subplanted in the film. This can explain the out-of-plane lattice expansion, which was also observed experimentally for Cr films. We argue that the positive stress of the Cr films implies that the dominant stress component is the tensile and it cannot be compensated by the compressive one caused by the subplantation of the Ar species.

Acknowledgment

This work has been supported by the Deutsche Forschungsgemeinschaft (WU 243/13).

References

[1] Hultman L 2000 *Vacuum* **57** 1
[2] Glocker D A and Shat S I 1995 *Handbook of Thin Film Process Technology* (Wilmington, Delaware: Institute of Physics)
[3] Navansek B, Panjan P and Milosev I 1997 *Surf. Coat. Technol.* **97** 182
[4] Bertrand G, Savall C and Meunier C 1997 *Surf. Coat. Technol.* **96** 323
[5] Barata A, Cunha L and Moura C 2001 *Thin Solid Films* **398–399** 501
[6] Ortmann S, Savan A, Gerbig Y and Haefke H 2003 *Wear* **254** 1099
[7] Fabis P M, Cooke R A and McDonough S 1990 *J. Vac. Sci. Technol.* A **8** 3809
[8] He X-M, Baker N, Kehler B A, Walter K C and Nastasi M 2000 *J. Vac. Sci. Technol.* A **18** 30
[9] Cunhaa L, Andritschky M, Pischow K and Wang Z 1999 *Thin Solid Films* **355–356** 465
[10] Jung M J, Nam K H, Jung Y M and Han J G 2003 *Surf. Coat. Technol.* **171** 59
[11] Schell N, Petersen J H, Bøttiger J, Mucklich A, Chevallier J, Andreasen K P and Eichhorn F 2003 *Thin Solid Films* **426** 100
[12] Almer J, Oden M, Hultman L and Hakansson G 2000 *J. Vac. Sci. Technol.* A **18** 121
[13] Oden M, Almera J, Hakansson G and Olsson M 2000 *Thin Solid Films* **377–378** 407
[14] Dasgupta A, Kuppusami P, Lawrence F, Raghunathan V S, Premkumar P A and Nagaraja K S 2004 *Mater. Sci. Eng.* A **374** 362
[15] Sarakinos K, Kassavetis S, Patsalas P and Logothetidis S 2005 *Mater. Res. Soc. Symp. Proc.* vol 843, pp T.7.8.1–T.7.8.6
[16] Petrov I, Myers A, Greene J E and Abelson J R 1994 *J. Vac. Sci. Technol.* A **12** 2846
[17] Wang Z, Cohen S A, Ruzic D N and Goeckner M J 2000 *Phys. Rev.* E **61** 1904
[18] Berg S and Nyberg T 2005 *Thin Solid Films* **476** 215
[19] Ziegler F, Biersack J P and Littmark U 1985 *The Stopping and Range of Ions in Solids* (New York: Pergamon) http://www.srim.org
[20] Meeker D *Finite Element Method Magnetics* version 3.2 http://femm.berlios.se
[21] http://www.genplot.com
[22] Pauleau Y 2001 *Vacuum* **61** 175
[23] Windischmann H 1987 *J. Appl. Phys.* **62** 1800
[24] Davis C A 1993 *Thin Solid Films* **226** 30
[25] Hoffman R W 1976 *Thin Solid Films* **34** 185
[26] Stoney G G 1909 *Proc. R. Soc. Lond.* A **82** 172
[27] Perry A J 1990 *J. Vac. Sci. Technol.* A **8** 3186
[28] Gudmundsson J T, Alami J and Helmerson U 2002 *Surf. Coat. Technol.* **161** 249

[29] Lieberman M A and Lichtenberg A J 1994 *Principles of Plasma Discharges and Materials Processing* (New York: Wiley)
[30] Debal F, Bretagne J, Dauchot J P, Hecq M and Wautelet M 2001 *Plasma Sources Sci. Technol.* **10** 30
[31] Depla D and De Gryse R 2004 *Surf. Coat. Technol.* **183** 190
[32] Severin D, Kappertz O, Kubart T, Nyberg T, Berg S and Wuttig M 2006 *Appl. Phys. Lett.* **88** 161504
[33] International Centre for Diffraction Data 1999 JCPDS Powder Diffraction File No 85-1336
[34] International Centre for Diffraction Data 1999 JCPDS Powder Diffraction File No 79-2159
[35] Winters F 1965 *J. Chem. Phys.* **43** 926
Winters F 1966 *J. Chem. Phys.* **44** 1472
[36] Gall D, Shin C-S, Spila T, Oden M, Senna M J H, Greene J E and Petrov I 2002 *J. Appl. Phys.* **91** 3589
[37] Lifshitz Y, Kasi S R and Rabalais J W 1989 *Phys. Rev. Lett.* **62** 1290
[38] Patsalas P, Gravalidis C and Logothetidis S 2004 *J. Appl. Phys.* **96** 6234
[39] Janssen G C A M and Kamminga J-D 2004 *Appl. Phys. Lett.* **85** 3086
[40] Christou C and Barber Z H 2000 *J. Vac. Sci. Technol.* A **18** 6
[41] Kusano E, Kobayashi T, Kashiwagi N, Saitoh T, Saiki S, Nanto H and Kinbara A 1999 *Vacuum* **53** 21
[42] Kadlec S, Quaeyhaegens C, Knuyt G and Stals L M 1997 *Surf. Coat. Technol.* **89** 177
[43] Martin N, Santo A M E, Sanjines R and Levy F 2001 *Surf. Coat. Technol.* **138** 77
[44] Fukushima K, Kusano E, Kikuchi N, Saito T, Saiki S, Nanto H and Kinbara A 2000 *Vacuum* **59** 586
[45] Weast R C (ed) 1988–1989 *Handbook of Chemistry and Physics* (Boca Raton, FL: CRC Press)
[46] Nakagura S, Kusunoki T, Kakimoto F and Hirotsu Y 1975 *J. Appl. Crystallogr.* **8** 65
[47] Kamminga J-D, de Keijser Th H, Delhez R and Mittemeijer E J 2000 *J. Appl. Phys.* **88** 6332
[48] Abadias G and Tse Y Y 2004 *J. Appl. Phys.* **95** 2414
[49] Koch R 1994 *J. Phys.: Condens. Matter.* **6** 9519
[50] Ensinger W 1997 *Nucl. Instrum. Methods Phys.* B **127–128** 796